Journal of Instrumentation

SiPM-based dual-ended-readout DOI-TOF PET module based on mean-time method

To cite this article: Y.B. Han *et al* 2019 *JINST* **14** P02023

Jinst

PUBLISHED BY IOP PUBLISHING FOR SISSA MEDIALAB

RECEIVED: *November 7, 2018*
REVISED: *January 19, 2019*
ACCEPTED: *February 6, 2019*
PUBLISHED: *February 19, 2019*

SiPM-based dual-ended-readout DOI-TOF PET module based on mean-time method

Y.B. Han,[a] H.G. Kang,[a,b] S.H. Song,[a] G.B. Ko,[c] J.S. Lee[c] and S.J. Hong[a,d,1]

[a] *Department of Senior Healthcare, Graduate School, Eulji University, 771 Gyeryong-ro, Jung-gu, Daejeon 34824, Republic of Korea*

[b] *Department of Radiation Measurement and Dose Assessment, National Institute Radiological Science, 4-9-1 Anagawa, Inage-ku, Chiba 263-8555, Japan*

[c] *Department of Nuclear Medicine, College of Medicine, Seoul National University, 101 Daehak-ro, Jongno-gu, Seoul 03080, Republic of Korea*

[d] *Department of Radiological Science, Eulji University, 553 Sanseong-daero, Sujeong-gu, Seongnam-si, Gyeonggi-do 13135, Republic of Korea*

E-mail: hongseongj@eulji.ac.kr

[1] Corresponding author.

https://doi.org/10.1088/1748-0221/14/02/P02023

Abstract: Positron emission tomography (PET) with high resolution and high sensitivity is desirable for detecting cancers and neurological diseases. In this work, a depth-of-interaction (DOI)-time-of-flight (TOF) PET has been attempted to achieve both high spatial and high timing resolution. Dual-ended readout is a simple technique that can provide excellent timing and DOI resolutions and consistent signal arrival times, regardless of the DOI position along the scintillation crystal, as a mean-time method is used. A dual-ended readout DOI-TOF PET module consisting of a 6×6 array of $2 \times 2 \times 20\,\mathrm{mm}^3$ saw-cut cerium-doped lutetium-yttrium oxyorthosilicate (LYSO) crystals is constructed. Both ends of the LYSO crystal array are optically coupled to a multi-pixel photon counter (MPPC) with 4×4 channels. The sixteen MPPC outputs are reduced to four position signals using a charge division circuit (CDC) board, and the timing signal is extracted from the common cathode of the MPPC. The four position signals from the MPPC are digitized by a DRS4-based high-speed waveform digitizer with a sampling rate of 5 GSa/s. A ^{22}Na source is placed in front of a reference detector and at the side of the dual-ended readout DOI-TOF PET module in five steps of 2 mm, 6 mm, 10 mm, 14 mm, and 18 mm to measure the DOI, coincidence timing resolutions (CTRs), and mean-times. The full-width-half-maximums (FWHMs) of DOI resolutions and CTRs varied from 3.0 mm to 3.8 mm, with an average of 3.5 mm, and from 333 ps to 367 ps, with an average of 349 ps, respectively. The average of the slopes of the mean-time versus DOI position, for the 36 crystals, was -0.60 ± 1.68 ps/nm, which was consistent with the null value. The dual-ended readout DOI-TOF PET module based on the mean-time method produced both good DOI and CTRs, and consistent signal arrival times. The found solution would be the most advantageous in the small aperture PET systems, such as those for brain and breast imaging.

Keywords: Gamma camera, SPECT, PET PET/CT, coronary CT angiography (CTA); Scintigraphy and whole-body imaging

Contents

1 Introduction

Positron emission tomography (PET) provides physiological information by quantitatively measuring nuclear tracer uptakes and monitoring relative changes over time as physiological status progresses. High resolution and high sensitivity are highly desirable characteristics in PET for detecting cancers and neurological diseases such as Alzheimer's disease. The depth-of-interaction (DOI) measurement can provide high spatial resolutions even at the peripheral regions of the PET field-of-view (FOV) by reducing the parallax error. In particular, the DOI information is useful for brain- and breast-dedicated PET systems, which have relatively small diameters, compared to a whole-body PET scanner. On the other hand, the time-of-flight (TOF) technique can increase the signal-to-noise ratio (SNR) of the reconstructed PET images [1], which reduces the scan time without compromising the image quality, when compared to a non-TOF PET scanner [2]. Therefore, the DOI-TOF technique has the potential to improve the image quality of small aperture PET systems such as those for brain and breast imaging. Even though PET image reconstruction using a point spread function (PSF) can improve the spatial resolution at the peripheral regions of the PET FOV, a substantial effort is required for calibration. For this reason, many DOI PET detectors such as the multilayer scintillator arrays [3], monolithic scintillator detectors [4], and dual-ended readouts of pixelated scintillators [5] have been developed to obtain high timing and high spatial resolution, simultaneously. A monolithic scintillator reduces the inter-crystal dead space and achieves good DOI correction; however, the spatial resolution at the edges of the crystal is slightly degraded [6, 7]. Furthermore, the calibration of monolithic-scintillator-based PET detectors requires complicated procedures [8]. Recently, single-ended readout DOI-TOF PET detectors were developed to provide both TOF and DOI information, using a pulse-shaped discrimination [9, 10] or stair-shaped reflector methods [11]. However, the DOI resolution was greater than five millimeters, as the DOI step was limited by the number of crystal layers. The dual-ended readout method can obtain DOI resolutions less than three millimeters while preserving the timing resolution [12], and the mean-time method can be used to minimize the arrival time difference along the crystal, compared to single-ended readout detectors [13]. A small animal PET detector module using dual-ended readout and $0.953 \times 0.953 \times 20\,\text{mm}^3$ LYSO crystal with $BaSO_4$ reflector resulted in energy resolution of $12.9 \pm 2.3\%$, DOI resolution of 2.35 ± 0.17 mm, and timing resolution of 0.68 ± 0.04 ns [5]. The same group achieved energy resolution of $21.0 \pm 3.0\%$, DOI resolution of 1.84 ± 0.18 mm, and timing resolution of 1.23 ± 0.14 ns with a smaller $0.498 \times 0.498 \times 20\,\text{mm}^3$ LYSO crystal size [14]. Another group reported energy resolution of $21.8 \pm 5.8\%$, DOI resolution of 3.8 ± 1.2 mm, and timing resolution of 1.23 ± 0.10 ns with a $0.445 \times 0.445 \times 20\,\text{mm}^3$ LYSO crystal size [15]. A PET detector module using a crystal size of $1.55 \times 1.55 \times 20\,\text{mm}^3$ resulted in energy resolution of $12.8 \pm 1.5\%$, DOI resolution of 2.90 ± 0.15 mm, and timing resolution of 1.14 ± 0.02 ns with 0.445 mm width LYSO crystal [16]. In our previous study [13], the mean-time method to minimize the arrival time difference along the crystal has been demonstrated with a single crystal read out at both ends. In this study, the performance of a dual-ended readout DOI-TOF PET module consisting of a 6×6 array of $2 \times 2 \times 20\,\text{mm}^3$ saw-cut cerium-doped lutetium-yttrium oxyorthosilicate ($Lu_{1.9}Y_{0.1}SiO_5$: Ce, LYSO) crystals is evaluated for use in a DOI-TOF high-resolution PET.

2 Materials and methods

2.1 Dual-ended readout DOI-TOF PET module

The dual-ended readout DOI-TOF PET module consisted of a 6×6 array of LYSO crystals, each end of which was attached to a multi-pixel photon counter (MPPC) (Hamamatsu photonics, S13361-3050NE-04, Japan), as shown in figure 1a. The MPPC requiring a single bias voltage consists of a 4×4 channels. The "MPPC" is one of the brand names, among which "silicon photo-multiplier (SiPM)" is more widely used. "SiPM" and "MPPC" are interchangeably used in this paper. A single pixelated LYSO crystal in the 6×6 array has a dimension of $2 \times 2 \times 20\,\text{mm}^3$. The four side surfaces of the crystal were unpolished while the two side surfaces (top and bottom) were polished (Epic crystal Co., LTD. Shanghai, China) to improve the light-collection efficiency. A 100 μm thick barium sulfate ($BaSO_4$) reflector [2] was used to optically isolate the LYSO crystals, which resulted in a crystal pitch of 2.1 mm, as shown in figure 1b. The LYSO crystal array was optically coupled to the SiPM array using optical grease (BC 630, OKEN, Japan). The refractive indices were 1.81 for LYSO, 1.55 for MPPC and 1.465 for optical grease, respectively.

2.2 Characterization of reference detector

A reference detector was used to obtain coincidence events with the dual-ended readout DOI-TOF PET module for the measurement of the DOI, coincidence timing resolutions (CTRs), and mean-

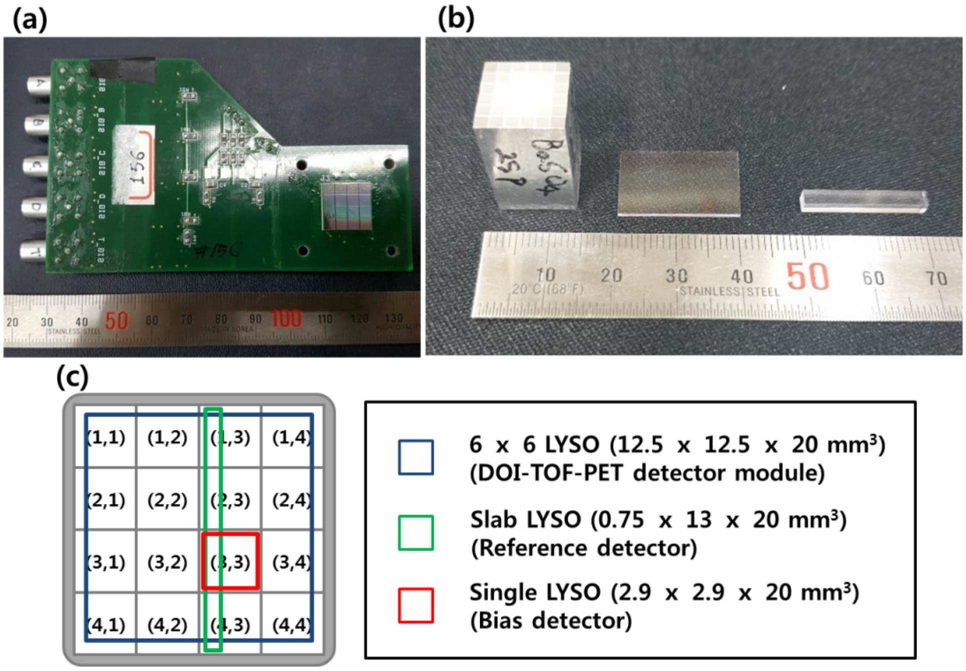

Figure 1. Front-end circuit board and crystals for the dual-ended readout DOI-TOF-PET module, reference and bias detector: 4×4 MPPC array with the front-end circuit (a), saw-cut 6×6 LYSO array painted with a $BaSO_4$ reflector for the dual-ended readout DOI-TOF-PET module, the polished LYSO slab for the reference detector, and the LYSO crystal for bias determination (b), and crystal positions of the various detectors on the sensitive area of the 4×4 MPPC detector (c).

times. The reference detector was constructed with a $0.75 \times 13 \times 20\,\mathrm{mm}^3$ LYSO crystal slab (Epic crystal CO., LTD. Shanghai, China) attached to a MPPC (Hamamatsu photonics, S13361-3050NE-04, Japan). The LYSO crystal slab was wrapped with Teflon tape (figure 1b). The LYSO crystal size ($0.75 \times 13 \times 20\,\mathrm{mm}^3$) of the reference detector was chosen to irradiate the 511 keV photons from a ^{22}Na source (10 µCi) on the crystal of the dual-ended readout DOI-TOF-PET module with an effective beam area of $1.5 \times 13\,\mathrm{mm}^2$, considering the distances of the source from the reference detector and the dual-ended readout DOI-TOF-PET module as shown in figure 2. The distance of the source from the dual-ended readout module and reference detector was 60 mm and 30 mm, respectively.

2.3 SiPM readout electronics

The dual-ended readout DOI-TOF-PET module and reference detector were placed in a light-tight temperature-controlled box to keep the temperature constant. As shown figure 2, initial 16 MPPC output signals from the 4×4 channels were reduced to four position signals (A, B, C, and D) by the charge division circuit (CDC) board. And these four signals were digitized by a DRS4-based high-speed waveform digitizer (DT5742B, CAEN S.p.A, Italy) [17, 18]. Each timing signal, which carried the timing information, was obtained from the common cathode of the SiPM. It was amplified with a gain of 12 using an amplifier (AD8000, Analog Device, Inc., MA), the bandwidth of which was 365 MHz (figure 2). The amplified signal was discriminated by a constant fraction

2019 JINST 14 P02023

discriminator (CFD N842, Caen, Italy) with a threshold of −0.5 V to produce a digital timing signal. The digital timing signals from the two MPPCs of the dual-ended readout DOI-TOF-PET module were required to produce a coincidence signal, with which the digital timing signal from the reference detector generated a trigger signal (TR0), as shown in figure 2.

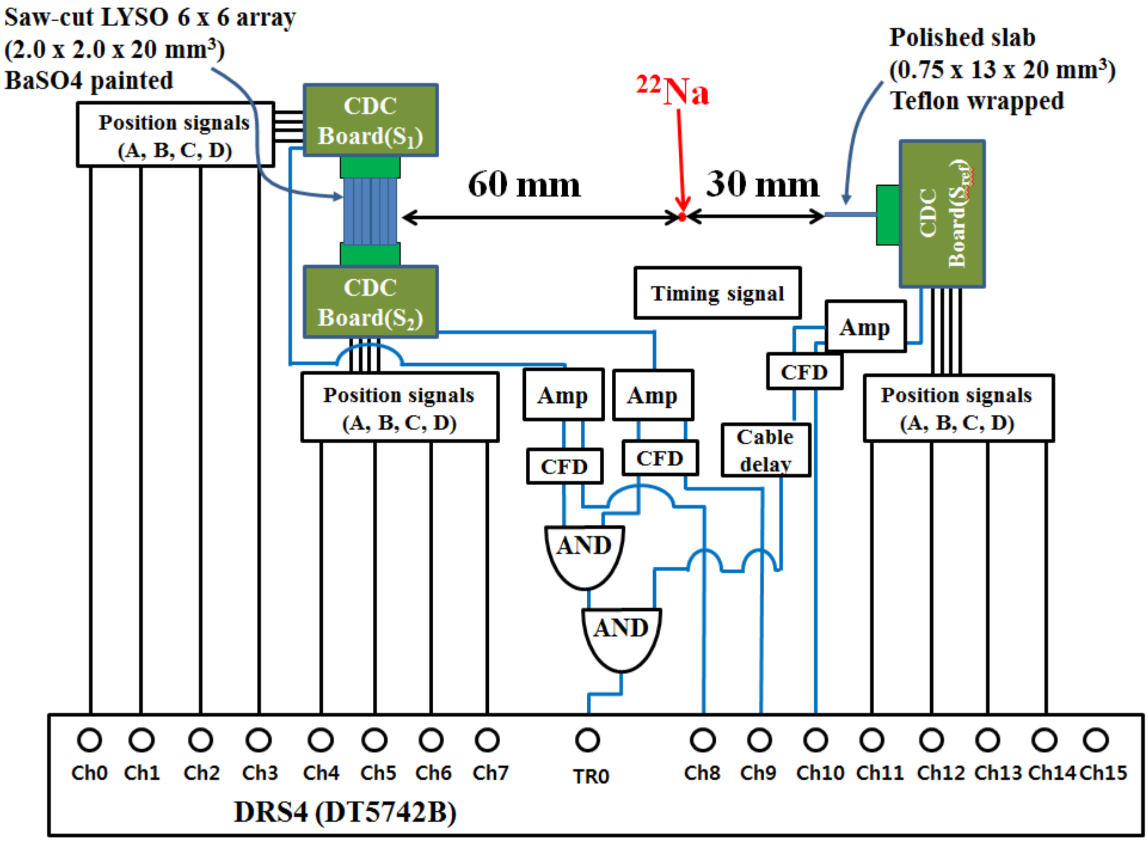

Figure 2. Dataflow diagram of experimental setup.

2.4 Determination of optimal bias for MPPCs

The MPPC with the 4×4 channels requires a single bias voltage. To find an optimal bias voltage for the MPPC, we assembled the MPPC with a $2.9 \times 2.9 \times 20\,\mathrm{mm}^3$ LYSO crystal and measured the coincidence timing and energy resolution, in a temperature-controlled box (20°C) by varying the bias voltage. The $2.9 \times 2.9 \times 20\,\mathrm{mm}^3$ LYSO crystal was attached to the (3, 3) single channel of MPPC (figure 1), from which the breakdown and optimal bias voltage were obtained.

A dataflow diagram similar to figure 2 was used to obtain position and timing signals. The breakdown voltages V_{ob} of the three SiPMs varied from 53.7 V to 53.9 V. The data of each SiPM were acquired by changing the operation voltage in 0.2 V steps (50,000 coincidence events per step) from the breakdown voltage.

To estimate the single timing resolution of the reference detector, we measured three sets of coincidence timing resolutions: those of SiPM (S_1) and SiPM (S_2), SiPM (S_1) and SiPM (S_{ref}), and SiPM (S_2) and SiPM (S_{ref}). The reference detector timing resolution was obtained by solving the following linear equation [13];

$$\begin{pmatrix} 1 & 1 & 0 \\ 1 & 0 & 1 \\ 0 & 1 & 1 \end{pmatrix} \begin{pmatrix} T^2_{\mathrm{SiPM(S_{ref})}} \\ T^2_{\mathrm{SiPM(S_1)}} \\ T^2_{\mathrm{SiPM(S_2)}} \end{pmatrix} = \begin{pmatrix} T^2_{\mathrm{SiPM(S_{ref})-SiPM(S_1)}} \\ T^2_{\mathrm{SiPM(S_{ref})-SiPM(S_2)}} \\ T^2_{\mathrm{SiPM(S_1)-SiPM(S_2)}} \end{pmatrix}. \tag{2.1}$$

2.5 Flood map and energy resolution analysis

The digitized values of the four position signals (A, B, C, and D) were used to calculate the gamma photon interaction position within the LYSO crystal array with the following equations:

$$\mathrm{X} = \frac{A + B - C - D}{A + B + C + D}, \qquad \mathrm{Y} = \frac{-A + B + C - D}{A + B + C + D}. \tag{2.2}$$

The gamma photon interaction position was used to generate a 2D flood image subsequently segmented to produce a Voronoi diagram [17]. Each segmented area in the Voronoi diagram was assigned to an individual crystal, for which the energy resolution, DOI resolution and CTR were obtained.

2.6 DOI resolution measurement

The gamma photons from the ^{22}Na source were irradiated to the side of dual-ended DOI-TOF-PET module to measure the DOI resolution, even though most gamma photons enter from the top of the PET detector module in actual PET scanners. The ^{22}Na source was placed in front of the reference detector and at the side of the dual-ended readout module (figure 2) at five distances of 2 mm, 6 mm, 10 mm, 14 mm, and 18 mm. The DOI positions were determined from the ratio of the signals of both SiPMs, as follows [13]:

$$Q_1 = A_1 + B_1 + C_1 + D_1, \qquad Q_2 = A_2 + B_2 + C_2 + D_2 \tag{2.3}$$

$$\text{DOI ratio} = \frac{Q_1 - Q_2}{Q_1 + Q_2} \tag{2.4}$$

where Q_1 and Q_2 represent the sum of the four position signals from each SiPM, respectively. The DOI resolution was measured using the full-width-half-maximum (FWHM) of a Gaussian fitting of the DOI ratio distribution [19, 20].

2.7 Coincidence timing resolution and mean-time measurement

As shown in figure 2, each end of the dual-ended readout DOI-TOF-PET module produces a timing signal. In order to estimate the photon arrival time more accurately, the timing signals read out by the DRS4 digitizer with a 5 GSa/s (i.e. 200 ps per TDC bin) sampling rate were further processed to obtain a 20 ps resolution per TDC bin using a cubic spline interpolation with an interpolation factor of 10 [21, 22]. The coincidence timing resolution was defined to be the FWHM of the distribution of the signal arrival time difference between the dual-ended readout DOI-TOF-PET module and the reference detector. The signal arrival timing resolutions were measured with various different threshold levels (1% to 40%). The best resolutions were obtained with a 3 ± 1% threshold level, and therefore, the 3% threshold level was applied in this study.

The mean-time method was used to obtain the signal arrival time at the dual-ended readout DOI-TOF-PET module [13]. The mean-time of the trigger signal at the dual-ended readout DOI-TOF-PET module was calculated using the following equation:

$$\text{Mean-time} = \frac{T_1 + T_2}{2} \tag{2.5}$$

where T_1 and T_2 are the signal arrival times at the two ends of the dual-ended readout module relative to the signal arrival time of the reference detector, respectively.

The mean-time in the distribution was calculated using the following equation:

$$\text{Mean-time} = \text{Peak value} \pm \text{Standard Deviation}/\sqrt{N} \tag{2.6}$$

where N is the number of events in the mean-time distribution. The average mean-time and its error in the 36 scintillation crystals were calculated using the following equations [23]:

$$\text{Average} = \frac{\sum_{i=1}^{M} a_i t_i}{\sum_{i=1}^{M} a_i}, \qquad a_i = \frac{1}{\sigma_{t_i}^2}\left(\sum_{i=1}^{M}\frac{1}{\sigma_{t_i}^2}\right)^{-1}, \qquad \text{Error} = \frac{1}{\sigma_{\langle t\rangle}^2} = \sum_{i=1}^{M}\frac{1}{\sigma_{t_i}^2} \tag{2.7}$$

where M is the total number of crystals in the 6×6 array and t_i is the mean-time in each crystal.

In order to verify that the mean-time is independent of the DOI position, the mean-times at five DOI positions over the 36 scintillation crystals were obtained. The linear regression method in the statistical package IBM SPSS V. 24 (IBM, U.S.A.) was used to calculate the slopes of the mean-time versus the DOI position over the 36 crystals.

3 Results

3.1 Determination of bias voltage

Figure 3 shows the coincidence time resolutions and energy resolutions of the SiPMs with a $2.9 \times 2.9 \times 20\,\text{mm}^3$ LYSO crystal versus the overvoltage. SiPM S_1 and S_2 were used in the dual-ended readout DOI-TOF-PET module, while SiPM S_{ref} was used in the reference detector.

For the SiPMs used for the dual-ended DOI-TOF-PET module, the coincidence timing resolutions were better at 8.1 V than at 7 V (figure 3a), while the energy resolutions did not depend strongly on the voltage between 6 V and 8 V (figure 3b). For the SiPM used for the reference counter, energy and coincidence timing resolutions were better at 7 V than at 8.1 V. Since the coincidence timing resolution of the dual-ended DOI-TOF-PET module was the most important parameter, we selected the overvoltage of 8.1 V to measure the coincidence time resolution, energy resolution, and mean-time.

3.2 Flood map and energy resolution

Figure 4 shows the flood maps of the dual-ended readout DOI-PET-TOF module, which were obtained with the ^{22}Na source placed at distances of 2 mm and 18 mm from the top crystal array. All crystals in the dual-ended module were well separated.

A flood map at the DOI position of 10 mm is shown in figure 5a along with a fishnet obtained using the Voronoi algorithm, and the energy resolution for each crystal was shown in figure 5b. The

2019 JINST 14 P02023

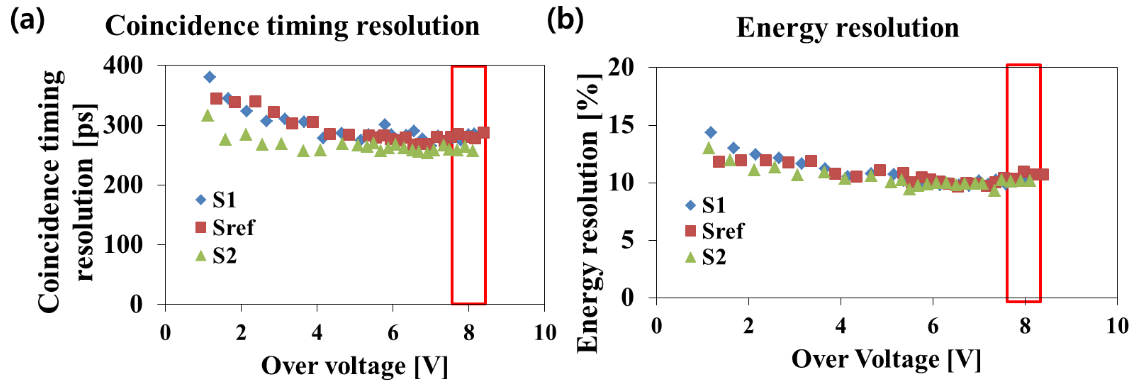

Figure 3. Coincidence timing resolution (a), and energy resolutions of SiPMs (b) as functions of the overvoltage.

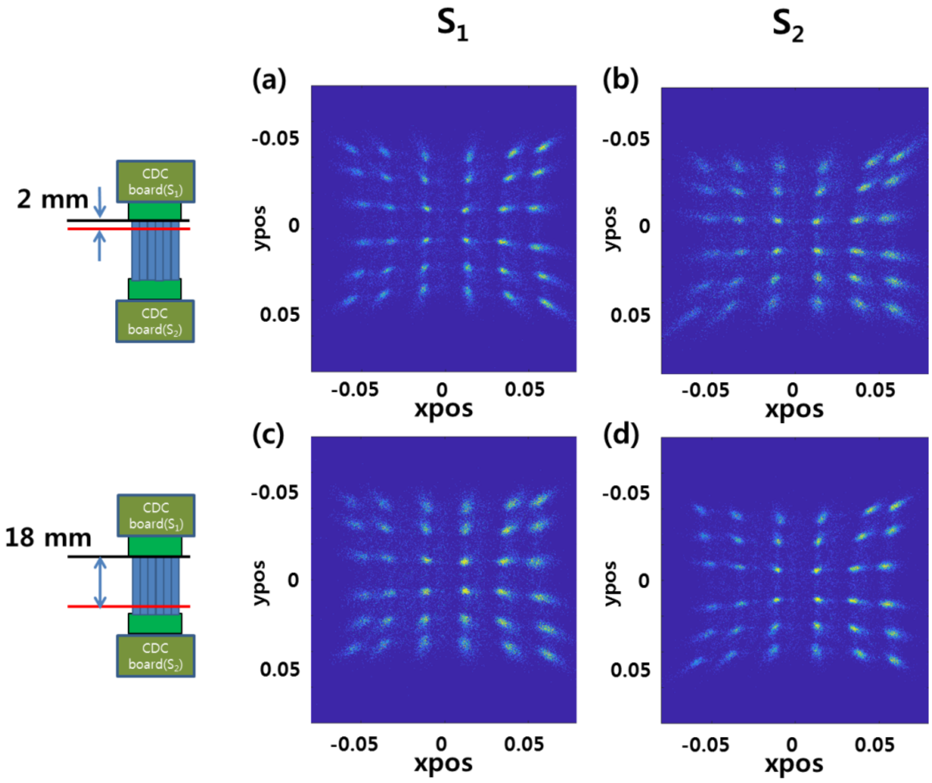

Figure 4. Flood maps at two different DOI positions of 2 mm and 18 mm from the top.

energy spectrum resolution of the circled crystal in figure 5b is shown in figure 5c, and it shows an energy resolution of 9.7%. The average energy resolution of the crystals shown in figure 5b was 11.7 ± 1.6%.

3.3 DOI resolution

Figure 6a shows the calculated DOI positions versus DOI steps and the average resolutions at five DOI steps of 2 mm, 6 mm, 10 mm, 14 mm, and 18 mm. The DOI in each crystal was obtained from

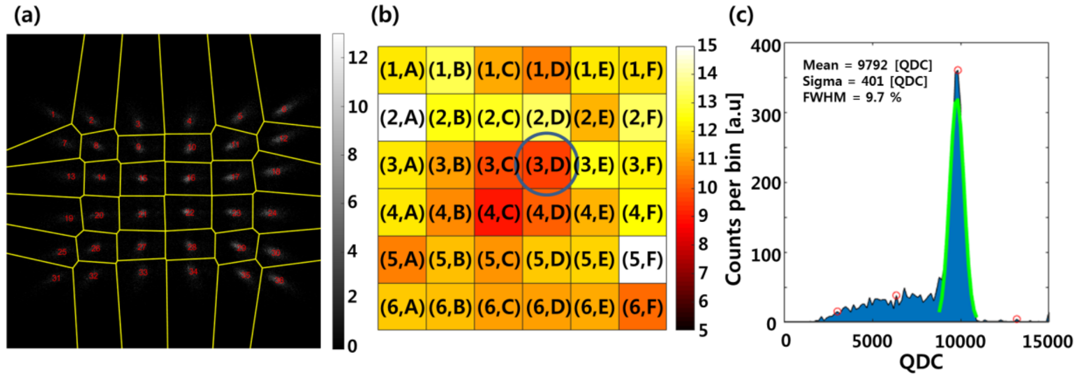

Figure 5. Flood map at the DOI position of 10 mm (a), energy resolution map (b), and energy spectrum of the circled crystal (c).

the DOI ratio by multiplying by a scale factor, which depends on the crystal position. The scale factors for the crystals painted in red are 31.8 in figure 6c, 48.8 in figure 6d, and 62.3 in figure 6e. The average DOI resolutions varied from 3.03 mm to 3.85 mm, with the average DOI resolution of 3.5 ± 0.3 mm (figure 6a). Figure 6b shows the average DOI resolutions over the 36 scintillation crystals.

Figures 6c, 6d, and 6e show the DOI ratio spectra at the five DOI positions at the crystal positions (1, F), (2, E), and (3, D), where crystal identification runs 1 through 6 in row, and A through F in column. The DOI ratio spectra differ quite a lot from each other, which resulted in the large different scale factors.

3.4 Coincidence timing resolution and mean-time

The coincidence timing resolution map corresponding to the crystal array map in figure 5a is shown in figure 7a. The average CTR was 349 ± 80 ps. Figures 7b, 7c, and 7d show timing spectra at different DOI distances at the crystal positions (1, F), (2, E), and (3, D) in the crystal map respectively.

Table 1 represents the mean-times at the five DOI positions and the averages of the crystals marked in figures 7b, 7c, and 7d, which were consistent within an error margin. Table 2 represents the average mean-times over the five DOI positions in the 6×6 crystal array. The differences in the average mean-times were caused by mostly the differences in the signal tracer lengths and capacitive loadings shown in figure 8.

Table 1. Mean-times at the five DOI positions (in ps) at the crystal position (1, F), (2, E), and (3, D).

Position	2	6	10	14	18	Ave.
(1, F)	714 ± 2.7	715 ± 3.5	715 ± 2.7	731 ± 2.6	749 ± 3.9	725 ± 7.0
(2, E)	874 ± 2.5	890 ± 2.4	882 ± 2.2	859 ± 2.4	862 ± 2.4	873 ± 5.3
(3, D)	901 ± 2.7	909 ± 2.4	923 ± 2.4	914 ± 2.2	884 ± 2.4	906 ± 5.4

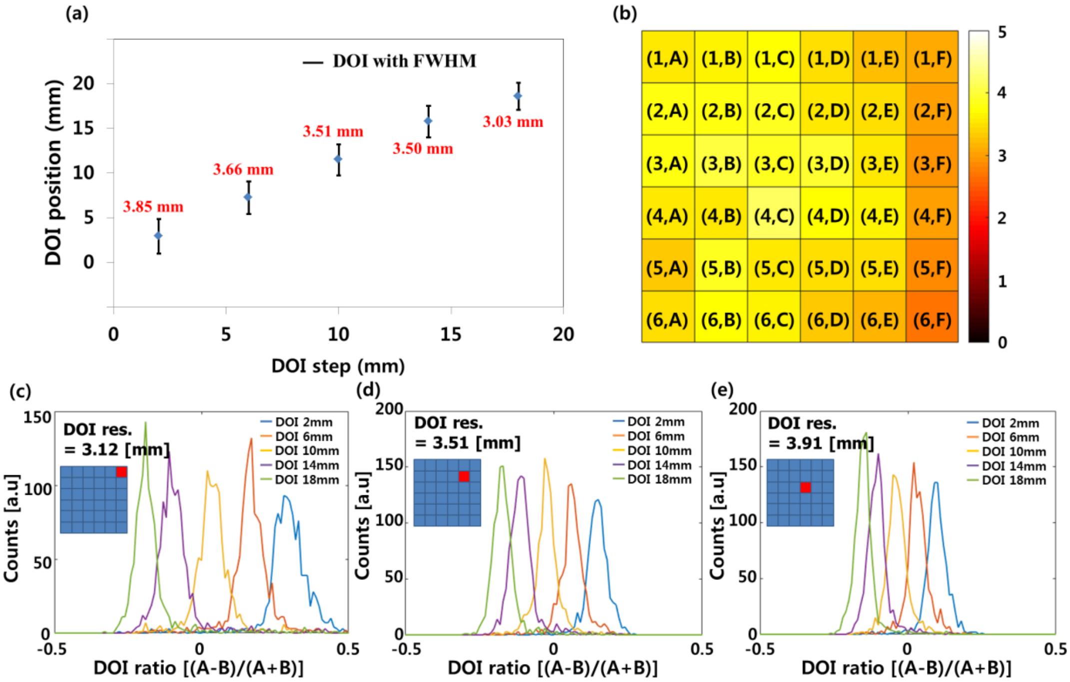

Figure 6. DOI resolutions at different ^{22}Na source positions (a), average DOI resolution map (b). DOI ratios of the DOI distance at the crystal positions (1, F) (c), (2, E) (d), and (3, D) (e) in the crystal map.

Table 2. Average mean-times over the five DOI positions in the 6 × 6 crystal array (in ps). Crystal identification runs 1 through 6 in row, and A through F in column.

	A	B	C	D	E	F
1	786 ± 9.7	851 ± 7.8	921 ± 6.4	920 ± 6.2	843 ± 6.2	725 ± 7.0
2	776 ± 8.1	881 ± 7.1	971 ± 6.5	963 ± 5.8	873 ± 5.3	739 ± 5.4
3	695 ± 7.3	812 ± 6.6	926 ± 5.8	906 ± 5.4	818 ± 5.2	670 ± 5.1
4	567 ± 8.1	671 ± 6.8	785 ± 5.6	780 ± 5.2	679 ± 5.1	520 ± 5.8
5	454 ± 7.9	551 ± 7.1	642 ± 6.2	632 ± 6	543 ± 5.3	415 ±5.6
6	324 ± 10	430 ± 8.2	511 ± 6.8	466 ± 6	409 ± 5.8	312 ± 5.4

4 Discussion

As shown in table 1, the mean-times along the 20 mm crystal at each crystal position of (1, F), (2, E), and (3, D) remained the same within an error margin, as the DOI distances changed, showing the independence of the mean-time along the crystal, as expected. The average of the slopes of the mean-times, as a function of the DOI position over the 36 crystals, was -0.60 ± 1.68 ps/mm, which was consistent with the null value [13]. The difference in the average mean-times among the crystals was caused by mostly the different signal travel lengths and capacitive loadings as described below.

Table 2 shows that the mean-times averaged over the five DOI positions in the 6 × 6 crystal array (in ps) differed from each other, which was caused by mostly the different signal travel lengths

2019 JINST 14 P02023

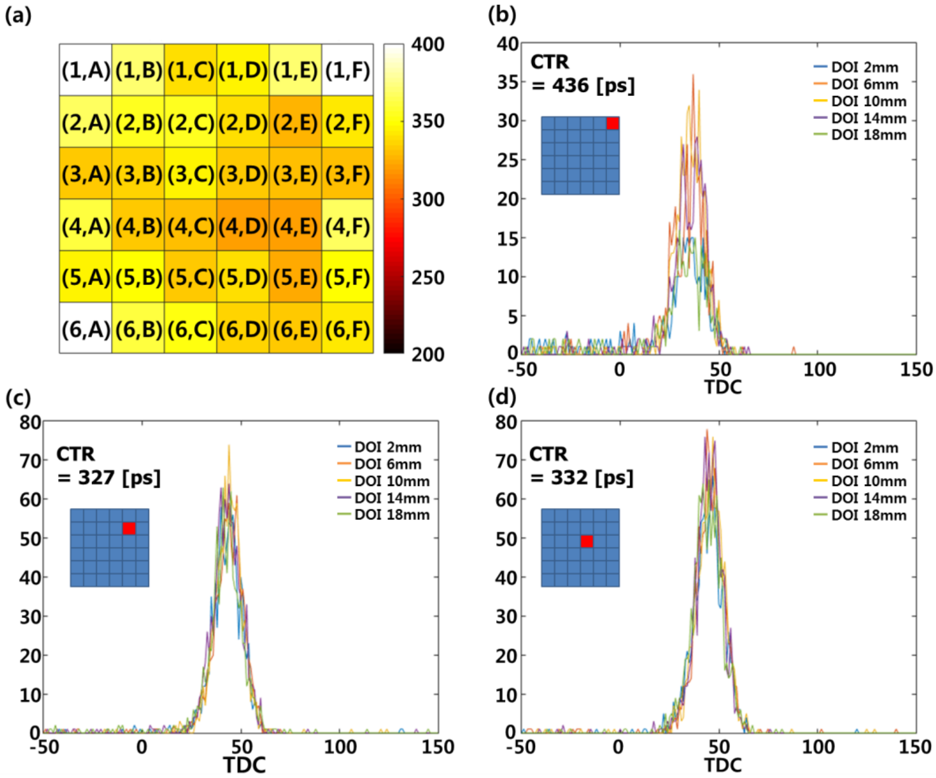

Figure 7. Coincidence timing resolution map (a). Timing spectra of the DOI distance at the crystal positions (1, F) (b), (2, E) (c), and (3, D) (d). Each TDC bin corresponds to 20 ps.

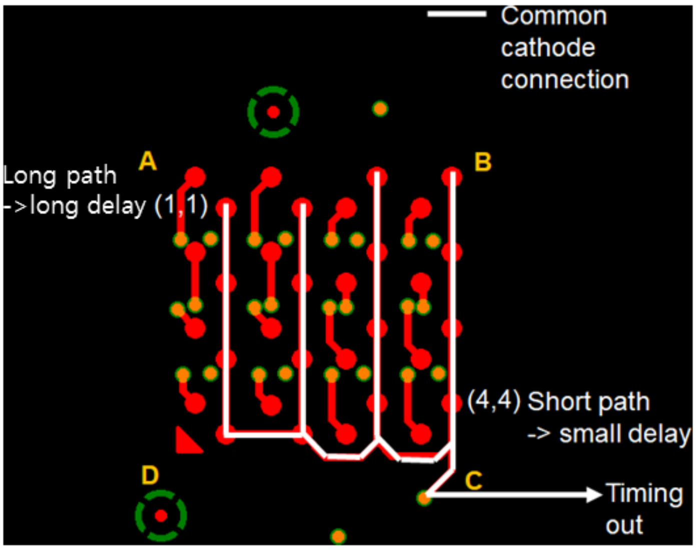

Figure 8. Path of SiPM's timing signal in the charge division board.

and capacitive loadings in the charge division board. In order to detect the coincidence in the PET system, it is highly desirable for each PET detector module to produce the same timing signal, independent of the crystal positions and DOIs. The signal travel length in the readout system has to be equalized to achieve this goal, and calibration of the arrival timing signal is also necessary to take into account the different capacitive loadings.

As the signal travel time is expected to be 120 ps in the 20 mm crystal with a refractive index of 1.8, the timing dependence on the DOI position along the crystal becomes non-negligible for PET systems with CTRs below 150 ps. The DOI position can be used to correct the signal arrival time dependence along the crystal. On the other hand, the mean-time method in the dual-ended readout PET module can provide the signal arrival time independent of the DOIs along the length of the crystal, but by using extra SiPMs compared to the single-ended readout PET.

Energy resolution is important for PET scatters to reject non-negligible scattered events in brain scans. The average energy resolution of the dual-ended readout DOI-TOF PET module was 11.7 ± 1.6% at the 10 mm DOI distance, the middle position of the crystal. Table 3 shows a summary of the coincidence timing and DOI resolutions at DOI distances of 2 mm, 6 mm, 10 mm, 14 mm, and 18 mm along the 20 mm crystal. The average coincidence timing and DOI resolutions were consistent over the 20 mm crystal, with an average of 349 ± 80 ps and 3.5 ± 0.3 mm, respectively.

Table 3. Coincidence timing resolution and DOI resolution for various DOI distances.

DOI distance [mm]	Coincidence timing resolution [ps]	DOI resolution [mm]
2	363 ± 42	3.9 ± 0.5
6	341 ± 38	3.7 ± 0.5
10	333 ± 31	3.5 ± 0.5
14	343 ± 26	3.5 ± 0.3
18	367 ± 48	3.0 ± 0.4

Energy resolutions, DOI resolution and CTR strongly depend on the crystal size, reflector and readout method. Previous studies using the dual-ended readout method for small animal PET systems achieved excellent DOI resolutions of 1.84 mm to 3.8 mm, but poor timing resolutions of 0.68 ns to 1.23 ns [5, 14, 15]. These studies used scintillation crystals with less than $1 \times 1\,\mathrm{mm}^2$ cross sectional area. This work aims for high DOI resolution and high CTR in small aperture PET systems such as those for brain and breast imaging by using the slightly larger crystal size of $2 \times 2 \times 20\,\mathrm{mm}^3$. Latest research on deep learning showed the potential for attenuation correction without computer tomography (CT) [24]. High spatial resolution brain- and breast-dedicated PET systems with DOI and TOF capability will be highly desirable for attenuation correction using deep learning in stand-alone PET systems. We have achieved significantly better timing resolution of 0.349 ± 0.08 ns and slightly worse DOI resolution of 3.5 ± 0.3 mm with a slightly larger crystal of $2 \times 2 \times 20\,\mathrm{mm}^3$.

Figure 6a and table 3 show that the DOI resolutions do not have the symmetry around the middle position of the crystal unlike the CTRs. The symmetric behavior of the DOI resolution and CTR for around the center is expected for perfect crystal condition and assembly of the dual-ended readout DOI-TOF PET module. The dual-ended readout DOI-TOF PET detector module may not have been perfect. Even though the similar tendency has been reported [16], this behavior needs to studied further with additional DOI-TOF PET detector modules in future. Figure 6b also shows that the DOI resolutions are better at the right side than at the left side, which also indicates imperfection in the dual-ended readout DOI-TOF PET module

5 Conclusion

The proposed SiPM-based dual-ended-readout DOI-TOF detector module using a 6×6 LYSO crystal array with a $2 \times 2 \times 20\,\text{mm}^3$ crystal size produced an energy resolution of $11.7 \pm 1.6\%$, DOI resolution of 3.5 ± 0.3 mm, and CTR of 349 ± 80 ps. We have shown it also has the potential of the signal arrival time independent of the DOI position. In the future, the optimal crystal treatment and reflector type will be investigated to further improve both the DOI and CTR.

Acknowledgments

This work was supported by grants from the Eulji University; National Research Foundation (NRF) of Korea of the Ministry of Science and ICT, Nuclear R&D Program (NRF-2016M2A2A4A03913619); and National Research Foundation (NRF) of Korea of the Ministry of Science and ICT, Nuclear R&D Program (NRF-2017M2A2A4A01071175).

References

[1] W.W. Moses, *Time of flight in PET revisited*, IEEE Trans. Nucl. Sci. **50** (2003) 1325.

[2] Z. Kuang et al., *Performance of a high-resolution depth encoding PET detector using barium sulfate reflector*, Phys. Med. and Biology **62** (2017) 5945.

[3] H. Uchida, T. Sakai, H. Yamauchi, K. Hakamata, K. Shimizu and T. Yamashita, *A novel single-ended readout depth-of interaction PET detector fabricated using sub-surface laser engraving*, Phys. Med. Biol. **61** (2016) 6635.

[4] G. Borghi, V. Tabacchini, R. Bakker and D.R. Schaart, *Sub-3 mm, near-200 ps TOF/DOI-PET imaging with monolithic scintillator detectors in a 70 cm diameter tomographic setup*, Phys. Med. Biol. **63** (2018) 155006.

[5] Z. Kuang et al., *Development of depth encoding small animal PET detectors using dual-ended readout of pixelated scintillator arrays with SiPMs*, Med. Phys. **45** (2017) 613.

[6] Z. Kuang et al., *A depth-encoding PET detector that uses light sharing and single-ended readout with silicon photomultipliers*, Phys. Med. Biol. **63** (2018) 045009.

[7] D.R. Schaart et al., *A novel, SiPM-array-based, monolithic scintillator detector for PET*, Phys. Med. Biol. **54** (2009) 3501.

[8] G. Borghi, B.J. Peet, V. Tabacchini and D.R. Schaart, *A 32 mm × 32 mm × 22 mm monolithic LYSO:Ce detector with dual-sided digital photon counter readout for ultrahigh-performance TOF-PET and TOF-PET/MRI*, Phys. Med. Biol. **61** (2016) 4929.

[9] C.M. Chang, J.W. Cates and C.S. Levin, *Time-over-threshold for pulse shape discrimination in a time-of-flight phoswich PET detector*, Phys. Med. Biol. **62** (2017) 258.

[10] G.B. Ko and J.S. Lee, *Single transmission-line readout method for silicon photomultiplier based time-of-flight and depth-of-interaction PET*, Phys. Med. Biol. **62** (2017) 2194.

[11] J.W. Son, M.S. Lee and J.S. Lee, *A depth-of-interaction PET detector using a stair-shaped reflector arrangement and a single-ended scintillation light readout*, Phys. Med. Biol. **62** (2017) 465.

[12] S. Seifert and D.R. Schaart, *Improving the Time Resolution of TOF-PET Detectors by Double-Sided Readout*, IEEE Trans. Nucl. Sci. **62** (2015) 3.

[13] H.G. Kang, G.B. Ko, J.T. Rhee, K.M. Kim, J.S. Lee and S.J. Hong, *A Dual-Ended Readout Detector Using a Meantime Method for SiPM TOF-DOI PET*, IEEE Trans. Nucl. Sci. **62** (2015) 1935.

[14] Z. Kuang et al., *Dual-ended readout small animal PET detector by using* 0.5 *mm pixelated LYSO crystal arrays and SiPMs*, Nucl. Instrum. Meth. **A 917** (2019) 1.

[15] J. Du et al., *Performance of a high-resolution depth-encoding PET detector module using linearly-graded SiPM arrays*, Phys. Med. Biol. **63** (2018) 035035.

[16] A. Kolb et al., *Development of a novel depth of interaction PET detector using highly multiplexed G-APD cross-strip encoding*, Med. Phys. **41** (2014) 081916.

[17] G.B. Ko and J.S. Lee, *Performance characterization of high quantum efficiency metal package photomultiplier tubes for time-of-flight and high-resolution PET applications*, Med. Phys. **42** (2015) 510.

[18] S. Ritt, R. Dinapoli and U. Hartmann, *Application of the DRS chip for fast waveform digitizing*, Nucl. Instrum. Meth. **A 623** (2010) 486.

[19] Y. Shao and R.C. Simon, *Dual APD array Readout of LSO Crystals: Optimization of Crystal Surface Treatment*, IEEE Trans. Nucl. Sci. **49** (2002) 649.

[20] Y. Yang et al., *Depth of interaction calibration for PET detectors with dual-ended readout by PSAPDs*, Phys. Med. Biol. **54** (2008) 433.

[21] G.B. Ko and J.S. Lee, *Delay grid multiplexing-simple time-based multiplexing and readout method for silicon photomultipliers*, Phys. Med. Biol. **61** (2016) 7113.

[22] G.B. Ko and J.S. Lee, *Single transmission-line readout method for silicon photomultiplier based time-of-flight and depth-of-interaction PET*, Phys. Med. Biol. **62** (2017) 2194.

[23] G.F. Knoll, *Radiation detection and measurements*, John Willey and Sons, Inc., New York U.S.A. (2010).

[24] D. Hwang et al., *Improving the Accuracy of Simultaneously Reconstructed Activity and Attenuation Maps Using Deep Learning*, J. Nucl. Med. **59** (2018) 1624.

2019 JINST 14 P02023